Contents lists available at ScienceDirect

Virology

journal homepage: www.elsevier.com/locate/virology

Coronavirus infection induces progressive restructuring of the endoplasmic reticulum involving the formation and degradation of double membrane vesicles

Elaine M. Mihelc [a,*], Susan C. Baker [b], Jason K. Lanman [a]

[a] Department of Biological Sciences, Purdue University, 915 W. State St. West Lafayette, IN, 47907, USA
[b] Department of Microbiology and Immunology, Stritch School of Medicine, Loyola University Chicago, 2160 South First Ave. Maywood, IL, 60153, USA

A B S T R A C T

Coronaviruses rearrange endoplasmic reticulum (ER) membranes to form a reticulovesicular network (RVN) comprised predominantly of double membrane vesicles (DMVs) involved in viral replication. While portions of the RVN have been analyzed by electron tomography (ET), the full extent of the RVN is not known, nor how RVN formation affects ER morphology. Additionally the precise mechanism of DMV formation has not been observed. In this work, we examined large volumes of coronavirus-infected cells at multiple timepoints during infection using serial-section ET. We provide a comprehensive 3D analysis of the ER and RVN which gives insight into the formation mechanism of DMVs as well as the first evidence for their lysosomal degradation. We also show that the RVN breaks down late in infection, concurrent with the ER becoming the main budding compartment for new virions. This work provides a broad view of the multifaceted involvement of ER membranes in coronavirus infection.

1. Introduction

Coronaviruses (CoV) are members of the *Coronaviridae* family of enveloped, positive-sense RNA viruses which include human pathogens Severe Acute Respiratory Syndrome Coronavirus (SARS-CoV), Middle East Respiratory Syndrome Coronavirus (MERS-CoV), and the recently emerged Severe Acute Respiratory Syndrome Coronavirus 2 (SARS-CoV-2). Like other positive-sense RNA viruses, CoV rearrange host cell organelle membranes to form neo-organelles involved in viral replication (reviewed in (Romero-Brey and Bartenschlager, 2014)). In CoV infection, replication takes place in connection with a virus-induced reticulovesicular network (RVN) consisting of double membrane vesicles (DMVs) and convoluted membranes (CM) (Gosert et al., 2002; Knoops et al., 2008; Snijder et al., 2020).

Significant work has been done to describe the morphology and role of viral and cellular proteins in CoV membrane rearrangements. The RVN for SARS-CoV has been described by electron tomography as DMVs, CMs, and ER which are connected via small membranous connections (Knoops et al., 2008). Recently, two cryo-ET studies have shown DMVs in their native state, both describing the structure in particular of the inner RNA density in unprecedented detail, and one describing a

previously unknown molecular pore in the DMV membrane (Wolff et al., 2020; Klein et al., 2020). Large numbers of DMVs have been observed in infected cells, and the RVN is understood to be quite extensive. An overall increase in membrane rearrangements over time was observed in a study which analyzed the type and number of various membrane rearrangements up to 10 hpi using thin section EM (Ulasli et al., 2010).

On the molecular level, the RVN is produced by the virally-encoded nonstructural proteins (nsps). Specifically, three nsps contain transmembrane domains which aid in membrane rearrangement. Co-expression of nsp3, nsp4, and nsp6 from SARS-CoV was found to be required and sufficient to produce membrane pairing, curvature, and double membrane vesicles, and a model was proposed whereby nsp3-nsp4 interactions produced pairing and curvature and nsp6 was involved in vesicle formation (Angelini et al., 2013, 2014). Three-dimensional imaging revealed that co-expression of nsp3 and 4 from either MERS-CoV or SARS-CoV produced zippered ER which wrapped into DMVs. (Oudshoorn et al., 2017).

In addition to nsps, cellular factors play a role in DMV formation. The RVN lacks traditional ER markers, but is continuous with the ER which is believed to be the membrane source of these structures (Knoops et al., 2008; Harcourt et al., 2004; Snijder et al., 2006; Kanjanahaluethai et al.,

2007; Oostra et al., 2007, 2008; Verheije et al., 2008; Reggiori et al., 2010). DMVs contain markers of ERAD tuning, including EDEM1, OS-9, and LC3-I (Reggiori et al., 2010). EDEM1 and OS-9 are luminal ER proteins which help in detection of misfolded proteins for ERAD (Molinari et al., 2003; Oda et al., 2003; Bernasconi et al., 2008; Christianson et al., 2008). Levels of these ERAD regulators are tightly controlled by ERAD tuning. In this process, EDEM1 and OS-9 are sequestered into LC3-I containing vesicles, termed EDEMosomes, which bud from the ER and are trafficked to lysosomes for degradation (Zuber et al., 2007; Fourn et al., 2009; Calì et al., 2008). Unlike EDEMosomes, CoV DMVs are bounded by two membranes, are connected to the ER via the RVN, and accumulate within the cell over the course of infection (Gosert et al., 2002; Knoops et al., 2008; Ulasli et al., 2010). It is not understood precisely how membrane pairing and the ERAD tuning pathway together form DMVs, or how DMVs ostensibly evade the degradative fate of EDEMosomes.

In addition to host cell membranes' involvement in CoV replication, they also play a role in assembly and budding of new virus particles (VP). CoV VP obtain their envelopes by budding into the lumen of the organelles of the secretory pathway. While the ER-Golgi intermediate compartment (ERGIC) is the major budding compartment, assembly of virus particles on the Golgi and ER has also been observed (Tooze et al., 1984; Krijnse-Locker et al., 1994). Tooze et al. suggested that the budding compartment changes over time and that the ER becomes the major budding compartment late in infection (Tooze et al., 1984). In SARS-CoV it was observed that late in infection, DMV inner vesicles were present within the lumen of the budding compartment (Knoops et al., 2008). The involvement of the ER membranes in both RVN formation and late stage envelopment raises questions as to how the ER houses both processes and how its morphology may change to reflect these disparate roles.

To address questions of RVN and ER morphology and DMV formation during CoV infection, a high-resolution, large volume imaging technique was needed. To date, large-scale ER structure in mammalian cells and yeast has been visualized using focused-ion beam milling scanning electron microscopy (FIB-SEM), serial block face SEM (SBF-SEM), or electron tomography (ET) (Puhka et al., 2007, 2012; West et al., 2011; Nixon-Abell et al., 2016). Three-dimensional analysis of small portions of the CoV RVN showed that the high resolution of electron tomography (ET) enabled visualization of double membranes as well as small membrane connections within the RVN (Knoops et al., 2008; Wolff et al., 2020; Klein et al., 2020). This resolution was required for our study. In order to achieve a large volume by ET, we utilized both a montage image collection and collected tomograms on serial sections, a strategy that has been used to image up to entire mammalian cells (Noske et al., 2008). The resulting volumes were approximately 30 times the volume of a single tomogram, and we refer to them as large volume tomograms (LVT).

In this work, we used large volume ET to perform a comprehensive morphological analysis of the RVN and ER at two distinct timepoints in the CoV Mouse Hepatitis Virus (MHV) infection. We show that the DMV life-cycle consists of budding from the ER, separating from the RVN, and trafficking to lysosomes for degradation. The final step leads to the breakdown of the RVN late in infection. The dynamic structure of the RVN over the course of infection exists concurrently with a shift in virus assembly from the ERGIC to the ER. Together, these data describe the highly dynamic nature of CoV infection within the cell, in particular in its interaction with the ER.

2. Results

2.1. Characterization of RVN and ER changes through the course of MHV infection

To establish a broad view of virus-related structures through the course of infection, confocal microscopy was performed on MHV-

infected 17Cl-1 cells at timepoints between 4 and 16 h post infection (hpi). To monitor the development of the replication-associated RVN, MHV strain A59 expressing GFP as a fusion with nsp3 (MHV-Δ2-GFP3 (Freeman et al., 2014)) was utilized. Nsp3 is one of three nonstructural proteins most directly involved in producing RVN-like membrane rearrangements, specifically through membrane pairing and proliferation (Angelini et al., 2013). Faint punctate fluorescence was observed at 4 hpi, located perinuclearly. Over time, the number of puncta as well as the fluorescence signal increased, with extensive RVN formation visible by 7 hpi (Fig. 1A). Nsp3 puncta did not appreciably coincide with the ER marker calreticulin. The ER itself appeared web-like and morphologically typical despite the presence of the RVN (Fig. 1A). As infection progressed, infected cells were increasingly present as multi-nucleate syncytia (Fig. 1A and Fig. S1A). Syncytia formation is initiated by expression of the S (spike) glycoprotein on the cell surface, which allows infected cells to fuse with one other (De Groot et al., 1989). By 12 hpi, nearly all infected cells were present in syncytia and the punctate fluorescence of the RVN had increased in intensity (Fig. 1A, Fig. S1A). Virus production peaks around 12 hpi (Fig. S1B). The RVN remained distinct from the ER throughout infection. At 12 hpi and beyond, brighter globular regions of ER were observed in addition to the typical ER structure (Fig. 1B, 12 hpi). These regions colocalized with viral M protein, the major membrane glycoprotein of MHV particles (Sturman et al., 1980). The presence of virus particles in the ER was only observed late in infection. At earlier timepoints, M protein showed strong Golgi localization (Fig. 1B and Fig. S2).

Based on the confocal data, samples were prepared for thin section electron microcopy at the same infection timepoints (4, 7, 10, 12, and 16 hpi). At 4 hpi, most cell cross-sections showed no signs of infection, but individual DMVs or small DMV clusters were occasionally observed (Fig. 2A–C). A distinct granular inner density was visualized in DMVs (Fig. 2B and C) which is believed to consist of dsRNA and replicase proteins. Visualization of the density was attributable to sample preparation by cryofixation and freeze substitution. In the literature to date, CoV DMVs appear empty unless prepared by these methods (Gosert et al., 2002; Knoops et al., 2008; Ulasli et al., 2010; Snijder et al., 2006; Goldsmith et al., 2004; Maier et al., 2013; de Wilde et al., 2013). During review of this manuscript, two studies providing unprecedented cryo-ET images of native-state DMVs was published, revealing the interior density to consist of relatively long filamentous structures consistent with dsRNA (Wolff et al., 2020; Klein et al., 2020). At 7 hpi, the most apparent change from 4 hpi was the large number of DMVs present in many cells (Fig. 2D and E). Additionally, virus particles (VP) were occasionally observed in Golgi cisternae and small membrane-bound compartments (Fig. 2F arrowheads). Overall, the number of DMVs and virus particles increased up to 10 hpi, consistent with the quantitative analysis by Ulasli et al. (Ulasli et al., 2010). By 12 hpi, VP were present in large numbers in the ER lumen (Fig. 2G–I) and assembling on the ER membrane (Fig. 2I arrowheads), while the RVN was present but less apparent (Fig. 2H arrowheads). At 16 hpi, the major characteristic of infected cells remained the ubiquitous presence of VP inside the ER; however, cells were fragile due to the advanced infection.

2.2. Collection of LVT and 3D characterization of the ER

Based on the confocal and ultrastructural time course analysis, we chose 7 hpi and 12 hpi as timepoints for further investigation into RVN structure, changes, and interaction with the ER over time. At 7 hpi, we observed extensive RVN, and the rate of RVN formation is expected to be maximal (Ulasli et al., 2010). Therefore we planned to use this timepoint to analyze RVN large-scale morphology, ER morphology changes in response to RVN formation, and to look for evidence of DMV biogenesis. At 12 hpi, virus production is at its maximum, and we observed extensive virus assembly in the ER. We planned to use this timepoint to explore how late-stage assembly affects the RVN and determine how extensive ER assembly is. In order to address these questions we
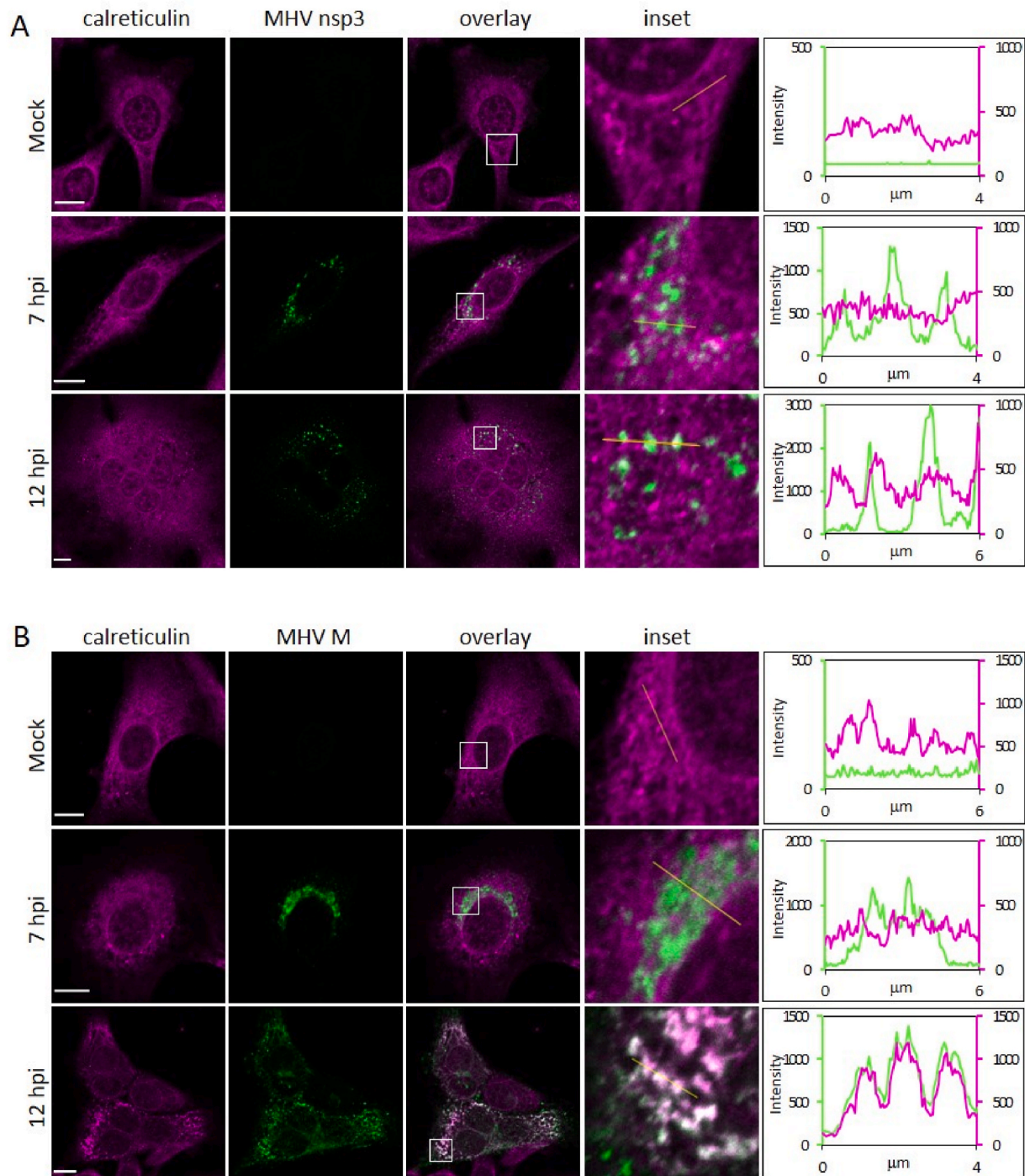
Fig. 1. Visualization of MHV proteins and the ER through the course of MHV infection. **(A)** 17Cl-1 cells were mock infected or infected with MHV-Δ2-GFP3 at an m. o.i. of 0.1, fixed at various timepoints, and processed for immunofluorescence detection of calreticulin as an ER marker. Nsp3 puncta remain independent from the ER throughout infection. At 12 hpi, cells are present as multi-nucleate syncytia and the ER exhibits increased punctation. **(B)** 17Cl-1 cells were mock infected or infected with MHV-A59, fixed at various timepoints, and processed for dual-labeled immunofluorescence detection of viral M protein and calreticulin. At 7hpi, M is mostly confined to the Golgi (see also Fig. S1). At 12 hpi, M and calreticulin have a high degree of colocalization in certain larger punctate regions. **Scale bars:** 10 μm.

collected serial-section large volume tomograms (LVT) of MHV-A59-infected 17Cl-1 cells cryofixed at 7 hpi and 12 hpi.

For the 7 hpi timepoint, we identified a cell which showed representative characteristics of the timepoint through several serial sections. The cellular area chosen included large numbers of DMVs, ER, and some VP. The area spanned the nucleus and the plasma membrane. A TEM image of one 250-nm section of the 7 hpi cell is shown in Fig. 3A with the area of collection outlined. A LVT was produced by a tilt series

acquisition combining montaged imaging at each tilt with collection of tomograms on eight serial sections. The final tomogram volume had dimensions of approximately 8 × 8 × 2 μm (Fig. 3B and Movie S1). Montaging and serial sectioning allowed the volume of the LVT to be approximately 32 times the volume of a single tomogram collected under these conditions.

In order to first analyze the structure of the endogenous ER, the rough ER from approximately half of the LVT was segmented using semi-
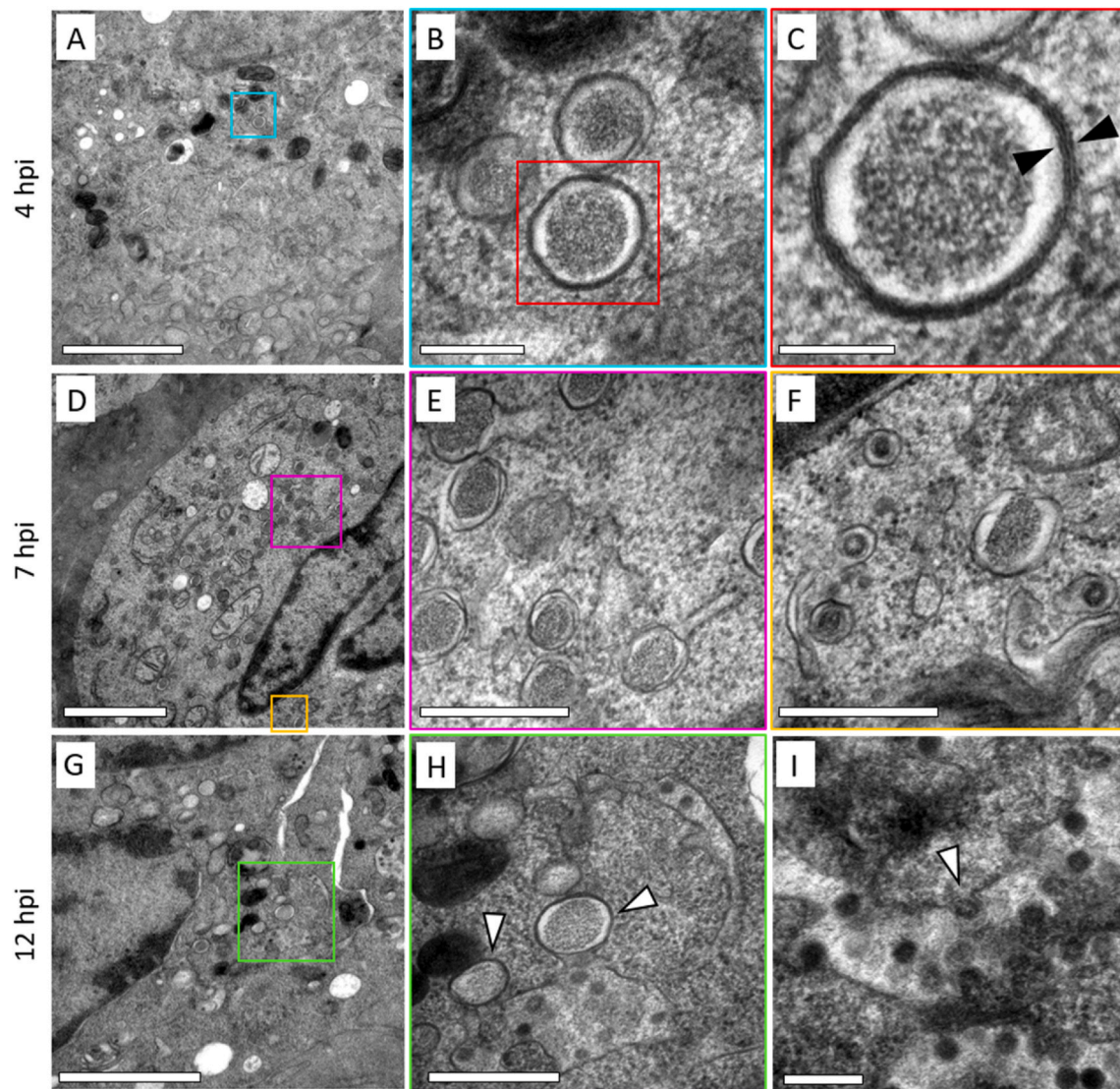
Fig. 2. Observations of thin sections from three timepoints during MHV infection. 17Cl-1 cells were infected with MHV-A59 at an m.o.i. of 10 for the stated times, followed by HPF and FS. Images are from 90-nm sections. **(A–C)** Early in infection (4 hpi), perinuclear DMVs and small clusters of DMVs are occasionally observed. Note the preservation of DMVs including the interior density as well as a double bilayer identified by three layers of stain (arrowhead in C). **(D–F)** At 7 hpi, large numbers of DMVs are observed throughout the cytoplasm, and enveloped virus particles in small vesicular structures is occasionally observed (arrowheads in F). **(G–I)** Late in infection (12 hpi), in addition to DMVs, virus particles are observed extensively in the ER lumen, including assembling particles on the cytoplasmic side of the ER (arrowhead in I). **Scale bars:** 2 μm (A, D, G), 200 nm (B, I), 100 nm (C), and 500 nm (E, F, H).

automated methods, and a 3D model was produced (Fig. 3C and D and Movie S1). The ER of the infected cell exhibited largely typical continuous, cisternal morphology; however, as reflected in the 3D view, many DMVs with outer membranes continuous with the ER were observed on the faces and edges of cisternae (Fig. 3E arrowhead). Another infection-induced change in the ER was the presence of paired membranes, including large cisternal regions with no detectible luminal space (Fig. 3F–I). While only four of these large paired cisternal regions were observed in the volume, such zippered ER (zER) has been observed routinely in gammacoronavirus and deltacoronavirus infection (Maier et al., 2013; Doyle et al., 2019). ZER has also been induced by the co-expression of MERS-CoV nsp3 and nsp4 (Oudshoorn et al., 2017). Overall, much of the morphology of the cisternal ER was preserved at 7 h post infection, despite the budding of relatively large double membrane vesicles. These observations confirm that the extensive RVN remains largely spatially distinct from the endogenous ER.

2.3. 3D characterization of RVN structures

To morphologically describe the RVN, we first analyzed the structure of DMVs and CM. A total of 659 DMVs were identified within the volume, defined as approximately spherical vesicles with an outer double bilayer, electron lucent layer, and a distinct inner density (Fig. 4A and B, Movie S2). A representative DMV was modeled by segmentation of the membranes and a thresholded isosurface of the inner density (Fig. 4B). Each DMV was segmented and its volume calculated. DMV volumes formed a unimodal distribution ranging from 1.4×10^5 nm^3 to 2.0×10^7 nm^3, equivalent to a diameter range of 64–334 nm, assuming spherical morphology. The mean DMV volume was 6.5×10^6 nm^3 (mean diameter = 225 nm, SD = 39 nm, n = 659) (Fig. 4C). Altogether, DMVs occupied 4.4 μm^3, equivalent to 3.4% of the tomogram volume. Consistent with what has been previously reported, DMVs had extensive membranous connections (Knoops et al., 2008; Wolff et al., 2020). We observed connections between DMVs and CM, ER, and other DMVs. CM were identified as densely curved membranes, often with DMVs
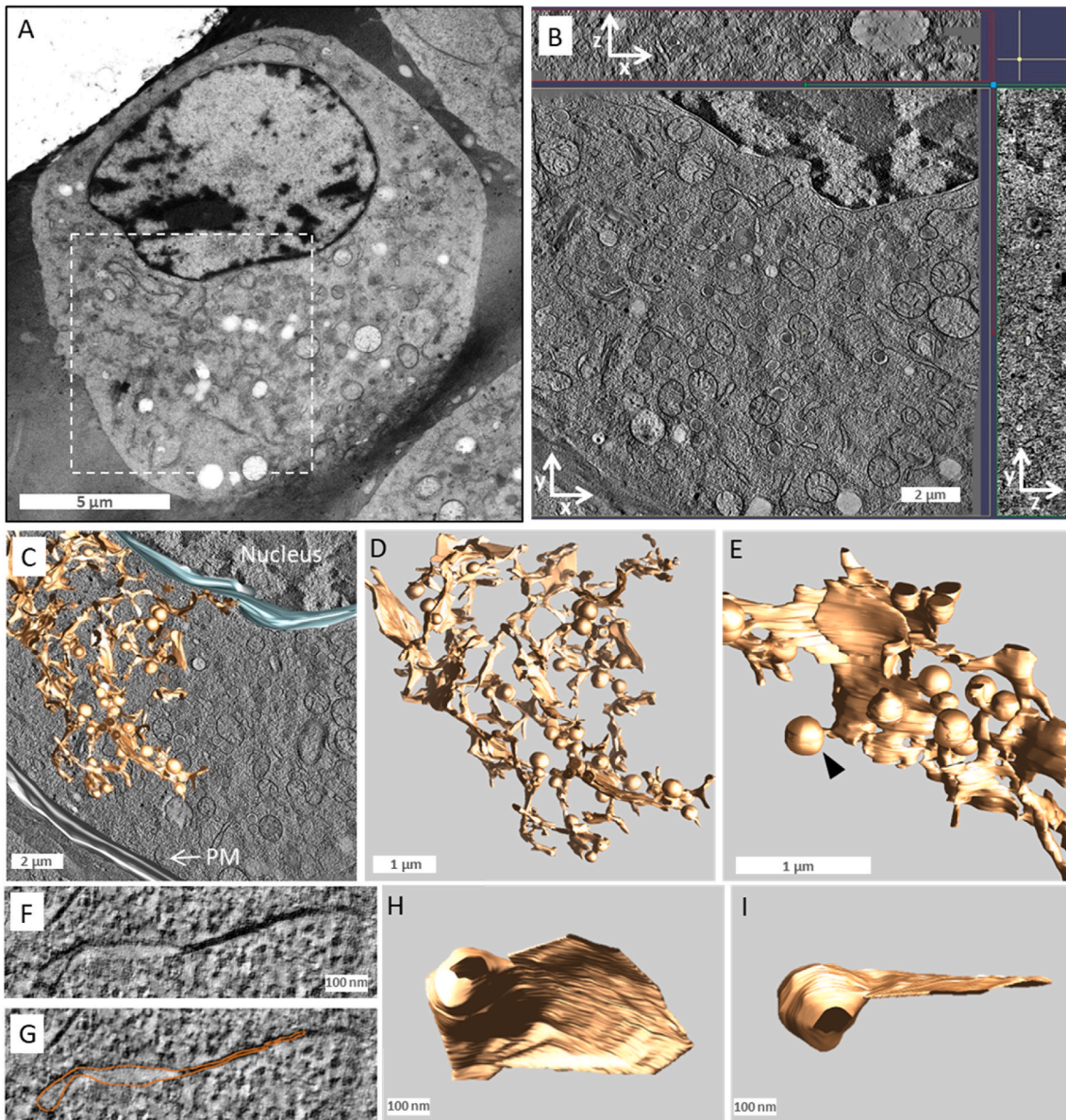
Fig. 3. Large volume tomography of an MHV-infected 17Cl-1 cell at 7 hpi. **(A)** TEM image of a 250-nm section collected on the Titan Krios at 300 kV. The cell used for LVT is shown with the outline of the approximate area for the tomogram collection. **(B)** Slices through the reconstructed LVT with the z-depth along the x and y axis shown along the top and right side, respectively. See also Movie S1. **(C–D)** 3D model of the ER produced by segmentation of approximately half the ER volume from the LVT. See also Movie S1. **(E)** A region of ER which illustrates the cisternal ER as well as DMVs with outer membranes continuous with the ER membrane (arrowhead). **(F)** Tomogram slice showing a region of cisternal paired ER, with segmentation trace shown in (G). **(H–I)** 3D models of the paired cisternal ER from (D).

surrounding and connected to them (Fig. 4D and E and Movie S3). Close examination of the CM structure on 2-nm thick virtual slices revealed short stretches of paired membrane which were difficult to trace in subsequent slices due to the high curvature (Fig. 4F arrowheads). An attempt at modeling the CM was achieved by tracing short double membrane segments on each slice using a tube (represented in IMOD as spheres). No regularly occurring pattern was visible in the 3D structure, but the highly curved, densely packed nature of the CM membranes was further established. A clear connection between the CM and ER and three DMVs was established for this CM (Fig. 4G). A study released during the preparation of this manuscript revealed that in addition to DMVs and CM, double-membrane spherules (DMSs) are present in the RVN, usually within the CM (Snijder et al., 2020). This study was the first observation of DMSs in betacoronavirus, including MHV. However, we did not observe DMSs in any of our 3D volumes or 2D images of MHV-infected 17Cl-1 or DBT cells.

2.4. The RVN at 7 hpi is an interconnected network of DMVs budding from the ER

In order to further describe the RVN and look for clues to RVN formation, we next examined the connections within the RVN. Because DMVs originate from the ER, we began with the DMVs most directly connected to the ER. Some DMVs had their outer membrane clearly continuous with the ER such that the inner DMV membrane contacted the lumen of the ER (Fig. 5A and Movie S4). These DMVs appeared to be fully enclosed vesicles budding out of ER cisterna to obtain their second membrane (Fig. 5A). They were observed budding from the face of cisternae (Fig. 5A iv black arrowhead) and cisternal edges (Fig. 5A iv, white arrowhead). Budding DMVs accounted for 126 of the 659 DMVs (19.1%). They were located throughout the imaged volume and were not found preferentially in any region of the cell or ER. Interestingly, no intermediates were observed which could be interpreted to represent
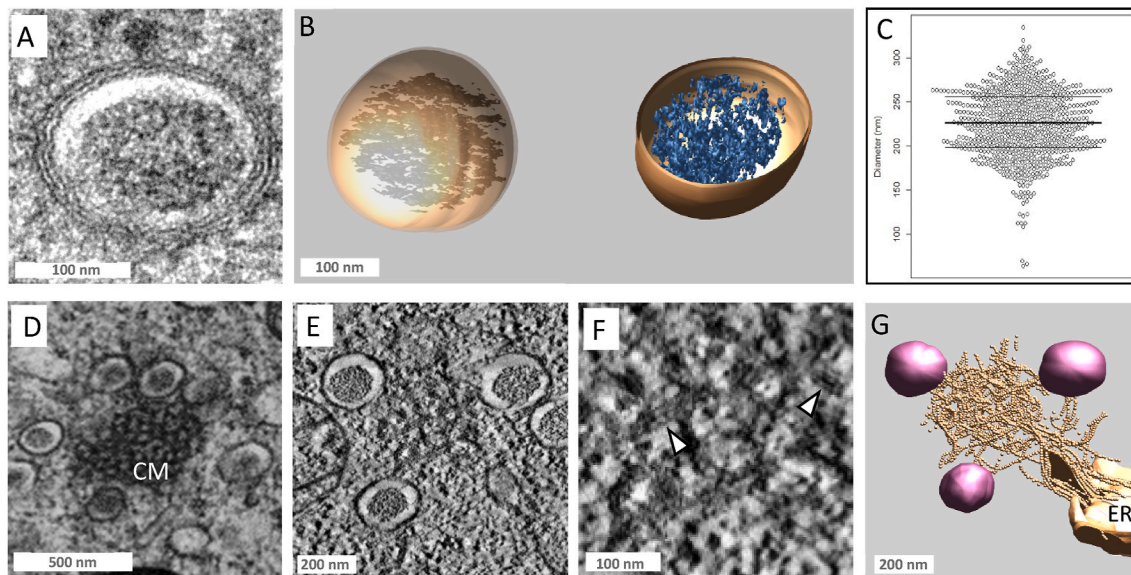
Fig. 4. 3D visualization of DMV and CM (A) TEM image of a 90-nm section of a DMV, clearly illustrating the double membrane, electron lucent ring, and electron dense core. **(B)** 3D visualization of a DMV from the LVT, with outer membrane (dark brown), tightly apposed inner membrane (light brown) and threshholded density of the inner core. **(C)** Plot of the distribution of DMV diameters calculated from segmented volumes. Thin lines represent the first and third quartile, and the thick line represents the mean value. **(D)** A TEM image of a 90-nm section containing convoluted membrane (CM) surrounded by DMVs. The section thickness allows the web-like structure to be observed. **(E)** A 2-nm tomogram slice of CM with paired membrane nature shown in the higher magnification image in **(F)**. **(G)** Segmenting the CM was attempted by drawing tubes (consisting of a series of spheres) along visible membrane segments on each slice. The membranes are continuous with DMV outer membranes as well as the ER.

earlier steps in DMV formation, including single membrane vesicles within the ER lumen or paired ER regions wrapping into DMV-sized vesicles.

A second category of DMVs also had outer membranes continuous with the ER; however, the membranes were pinched together to form a small paired region at the point of contact (Fig. 5B, especially Bii-arrowhead). Similar pinching connections were observed between two DMVs and between DMVs and CM (Fig. 5C). Altogether, 173 DMVs (26.2%) had pinching connections with ER, CM, or DMVs. A small number of DMVs (21, 3.2%) had two inner vesicles within a shared outer membrane (Fig. 5D). These vesicle packets have been observed in SARS-CoV and SARS-CoV-2 (Knoops et al., 2008; Klein et al., 2020). Nearly one-third of DMVs had two or more connections to the RVN, with DMVs having up to six total connections. In addition to contacting ER and RVN structures, 46 DMVs (7%) had outer membranes which contacted other organelle membranes including mitochondria and endo-lysosomal vesicles.

Another 126 DMVs (19%) had no visible connections to the ER, RVN or any other membrane, and thus were labeled "free" DMVs. An example is given showing nine virtual slices spaced at 20-nm intervals (Fig. 5E and F and Movie S5). No membrane structure comes within approximately 50 nm of the DMV in x, y, or z directions. The 3D view in Fig. 4G shows segmentation of the closest nearby structures, including the ER, a DMV, a microtubule, and two mitochondria.

The full tabulation of DMV connections is provided in Supplementary Table 1. Altogether, this analysis of the RVN at 7 hpi provides definition to the extensive nature of the RVN. DMVs have various degrees of connection to the ER/RVN, ranging from the entire outer membrane being continuous with the ER, to a large class of DMVs with no connections at all. These observations also provide visual evidence that one step in DMV formation includes budding from the ER.

2.5. ER structure is disrupted late in infection by virus assembly

After establishing the morphological characteristics of the RVN and ER at 7 hpi, near peak replication in the virus infection (van den Worm et al., 2011), we performed similar analysis at a late stage in infection, when the ER has an extensive role as a membrane source for newly forming VP. It was unknown how this new role affects the RVN or ER morphology. To address this, we collected an LVT from an MHV-A59-infected 17Cl-1 cell fixed at 12 hpi. A representative cell syncytium from this timepoint was selected, and a region of the cell was chosen which contained extensive areas of ER and RVN, showed VP in the ER lumen, and encompassed the nucleus and plasma membrane (Fig. 6A and B and Movie S6). A representative portion of the ER was segmented and visualized in 3D (Fig. 6C–E). While at 7 hpi, the ER largely maintained its cisternal morphology (Fig. 3C–E), at 12 hpi, the ER was herniated and globular and filled with VP (Fig. 6D). The globular regions were smaller than entire cisternae indicating that the cisternae are not only expanded to accommodate lumenal VP, but the cisternae are broken into smaller compartments as well (Fig. 6E). VPs were present in all regions of the ER lumen ranging from the outer nuclear membrane to the periphery of the cell (Fig. 6F). VP were frequently observed assembling on the cytoplasmic surface of the modified ER and budding into the ER lumen (Fig. 6G–I, arrowheads).

2.6. The RVN is broken down late in infection

In addition to changes in the ER, distinct changes in the RVN were observed between 7 and 12 hpi. No CM or zER were present in the 12 hpi volume. DMVs were segmented and their number, size and connections were analyzed as previously. The number of DMVs decreased prominently from the 7 hpi to the 12 hpi LVT. At the earlier timepoint, 5 DMVs were present per cubic micron of the volume, while at the late timepoint, only 0.7 DMVs/μm^3 were present. In both LVTs, DMVs were distributed throughout the ER and cellular volume (Fig. 7A and B). The types of connections within the RVN also changed over time, most notably free DMVs increasing from 19.1% to 46.9% of the total (Fig. 7C and Supplementary Tables 1 and 2). Additionally, DMVs with multiple connections decreased from 32% to 6% of the total, and at 12 hpi no DMVs with more than 2 connections were observed. Thus, between 7 and 12 hpi, the RVN breaks down in terms of number of DMVs, their
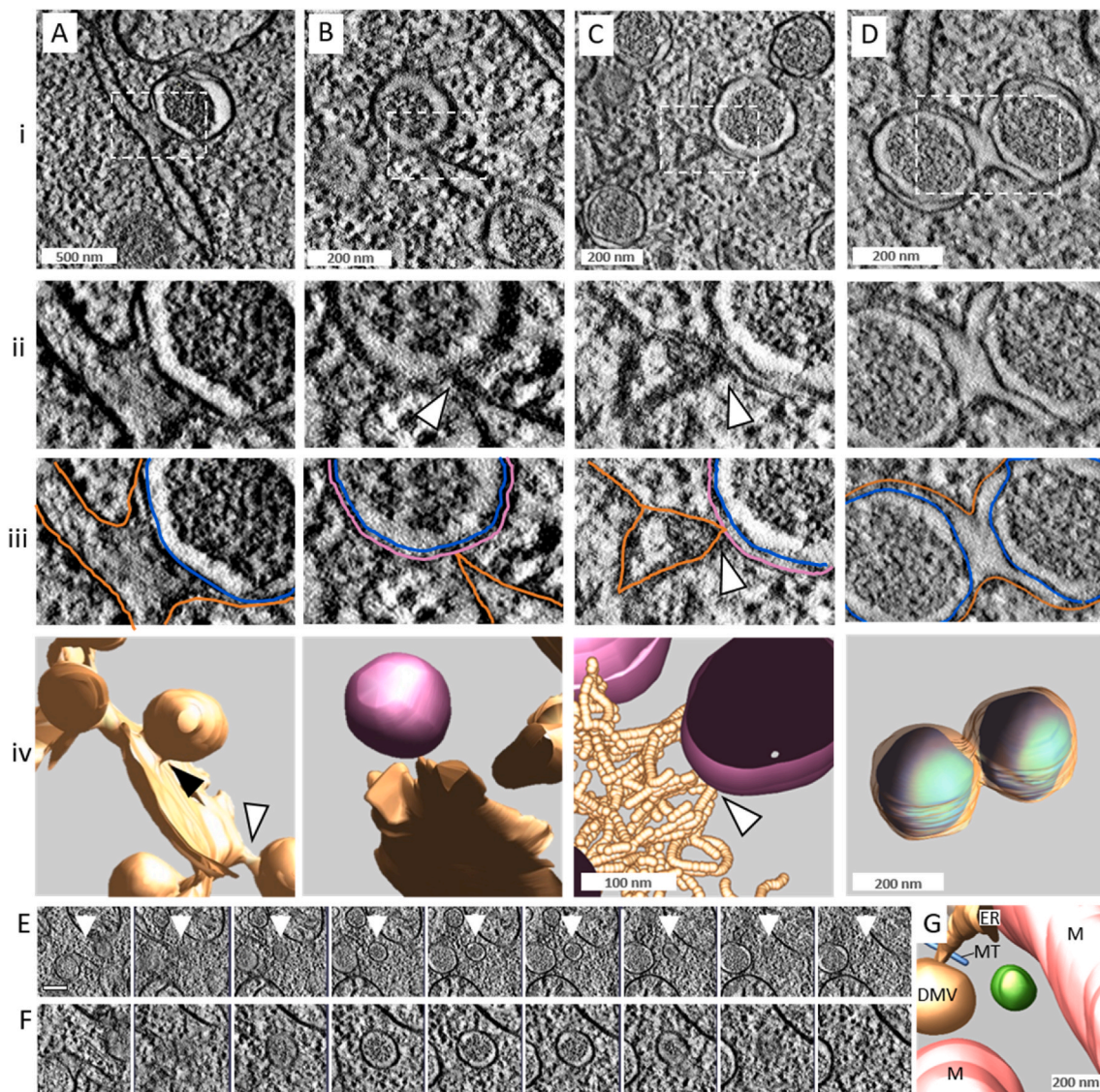
Fig. 5. LVT analysis of the RVN at 7 hpi. **(A–D)** Representative examples of the commonly observed membrane connections with DMVs, including budding DMVs with outer membrane continuous with the ER (A), Pinching DMV contacting the ER (B) or CM (C), and a DMV vesicle packet consisting of two inner vesicles which share an outer membrane (D). See also Movies S4-S5. **(E–F)** Serial tomogram slices with 20 nm spacing, illustrating the ability to detect DMVs which are not connected to any other membranes or organelles. Scale bar: 200 nm. **(G)** 3D model of the DMV shown in E-F in green, showing clear 3D separation from the nearest surrounding structures, including the labeled DMV, ER, mitochondria (M) and microtubule (MT).

connections, and loss of the CM structure.

Although every effort was made to choose representative areas of the cells for LVT collection, it was necessary to verify this RVN breakdown using a statistically relevant sample of thin sections. For each timepoint, DMV profiles from 25 cells were counted and cytoplasmic areas of the cells were calculated. From 7 to 12 hpi, the mean number of DMVs per cytoplasmic area decreased from 0.47 DMV/μm^2 to 0.24 DMV/μm^2 (p = 0.009). This verification of the RVN breakdown provides further evidence that the RVN is a more dynamic structure than previously understood.

2.7. DMVs are trafficked to lysosomes for degradation

In order to investigate RVN breakdown, we looked at host cell involvement in CoV infection. It has previously been shown that CoV DMVs contain cellular markers for ER-associated degradation (ERAD) tuning, namely EDEM-1, OS-9, and LC3-I (Reggiori et al., 2010). The vesicles involved in ERAD tuning are single membrane vesicles which bud from the ER and are rapidly trafficked to lysosomes for degradation

(Zuber et al., 2007; Fourn et al., 2009; Calì et al., 2008). Therefore, we hypothesized that ERAD tuning may play a role in the breakdown of the RVN. Because of the unique morphological characteristics of the DMV, we examined thin sections and the LVTs for visual evidence for lysosomal degradation of DMVs. We observed several examples of potential fusion events between a DMV and lysosome (Fig. 7D and E), as well as DMV-like objects present within lysosomes (Fig. 7F and G). Two potential mechanisms were also observed: both bilayers may fuse with the lysosomal membrane (Fig. 7E arrowheads), or the outer membrane alone may fuse leaving a single membrane vesicle inside the lysosome (Fig. 7G). DMVs were also observed associated with microtubules as would be expected of trafficking. The microtubule dependence of DMV movement has already been established; however, the interpretation was that DMVs were trafficking toward the RVN rather than away from it (Hagemeijer et al., 2010). In the 7 hpi volume, 15% of DMVs were located within 50 nm of a microtubule, and evidence of potential connections were observed (Fig. 7H–J).

To further test the hypothesis that CoV DMVs are degraded by ERAD tuning, the fusion of vesicles with lysosomes was blocked using
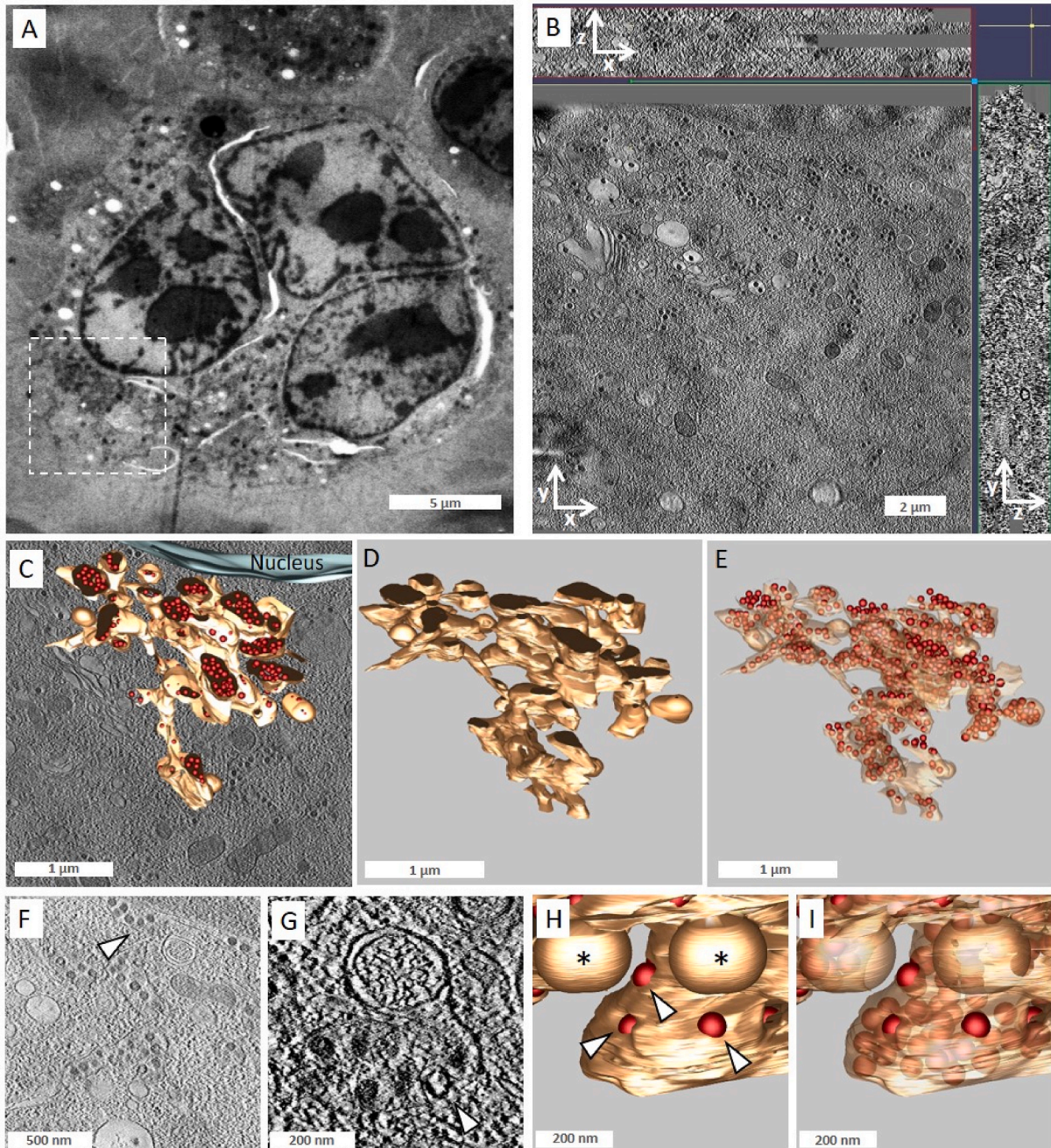
Fig. 6. ER morphology changes late in infection. **(A)** TEM image of a 250-nm section collected on the Titan Krios at 300 kV. MHV infected 17Cl-1 cells were fixed at 12 hpi and processed for ET. The cell (syncytium) chosen for LVT is shown along with the outline of the approximate area for the tomogram collection. **(B)** Slices through the reconstructed LVT with the z-depth along the x and y axis shown along the top and right side, respectively. See also Movie S6. **(C)** 3D model of a segmented portion of ER with enveloped VP (red), superimposed on a slice from the tomogram. **(D)** View of the globular ER structure without the virus particles. **(E)** Transparent view of the ER displaying the dense packing of VP within its lumen. **(F)** A tomogram slice demonstrating the presence of VP in the ER, including the nuclear envelope (arrowhead) and globular regions of ER. **(G)** Tomogram slice showing a region of ER with a budding DMV and inner budded VP as well as an assembling VP (arrowhead). **(H–I)** 3D model views of the region of ER shown in (G) with budding DMVs (asterisks) along with assembling VP (arrowheads).

chloroquine (CQ). CQ inhibits turnover of ERAD tuning proteins (Calì et al., 2008). 17Cl-1 cells were infected with MHV-A59 and the infection was allowed to progress for 7 h in order to allow the RVN to form. At 7 hpi, CQ was added to a final concentration of 100 μM. At 12 hpi, cells were cryofixed and processed for EM. DMV numbers from 25 cell cross sections were compared to data from untreated cells at 7 hpi and 12 hpi. In untreated cells, the mean number of DMV/μm^2 decreased from 0.47 to 0.24 from 7 to 12 hpi. CQ treated cells at 12 hpi contained 0.64 DMV/μm^2, nearly three times the number of DMVs present without

treatment (p = 0.001, Fig. 7K). Together these results reveal that trafficking of DMVs to lysosomes for degradation contributes to the breakdown of the RVN late in CoV infection.

2.8. The MHV budding compartment shifts through the course of infection

After observing the major changes that occur in the ER and RVN late in infection, we next examined the concurrent changes occurring in virus envelopment. Earlier in this study, we established that the M
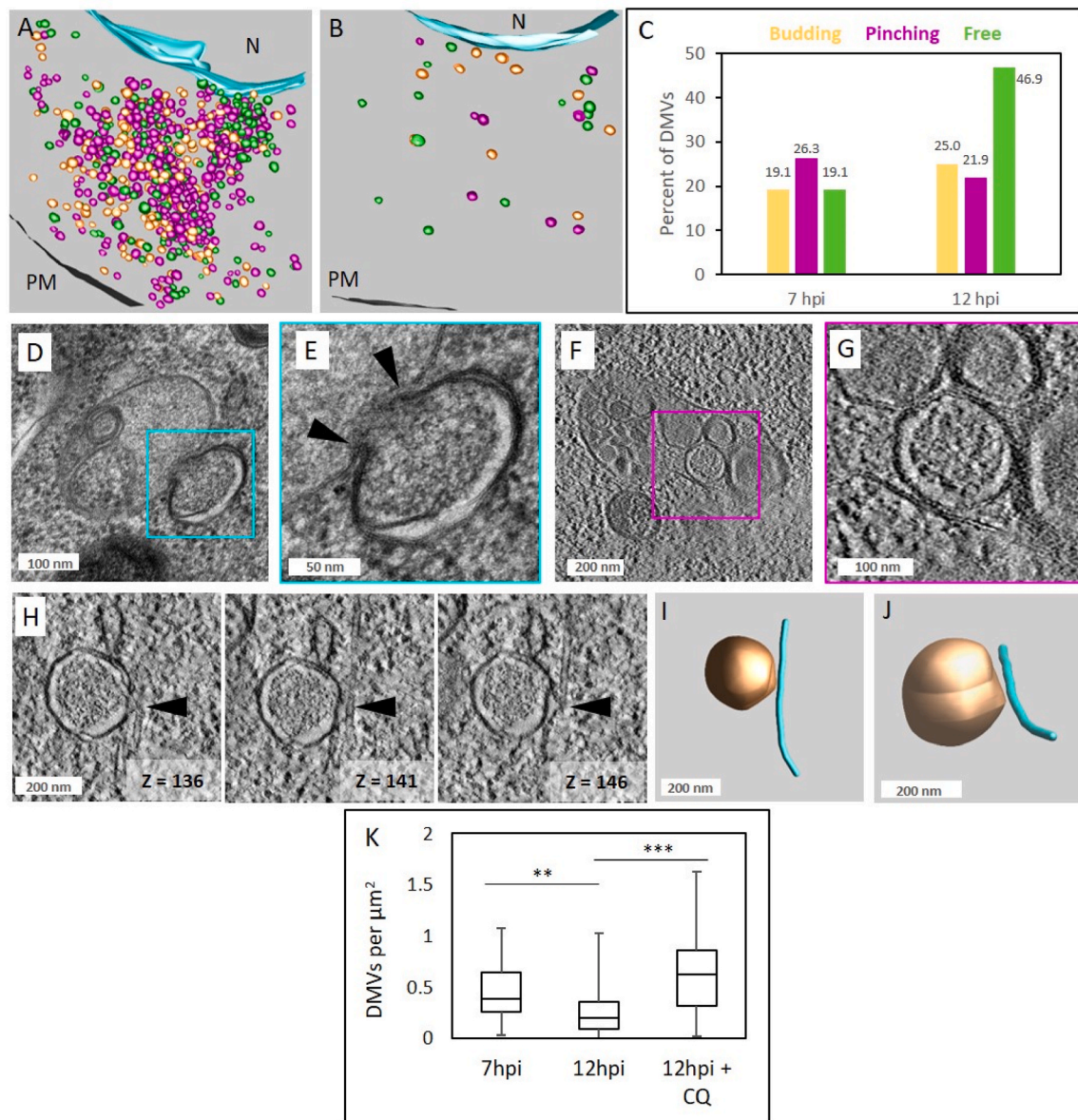
Fig. 7. The RVN is broken down late in infection and DMVs are trafficked to lysosomes. **(A–C)** Overview of the segmented DMVs present at 7 hpi (A) and 12 hpi (B) which are color-coded based on their classification as budding (yellow), pinching (magenta) or free (green). The nucleus (N) is shown in blue and the plasma membrane (PM) in grey. The proportion of DMVs in each of the classifications is shown graphically in (C). Only DMVs with single connections or no connections were included. **(D–E)** Thin section TEM images of a DMV fusing with a lysosome. Both membranes appear to be merging with the lysosomal membrane at two distinct points indicated by arrowheads in E. **(F–G)** Tomogram slices showing a single-membrane vesicle with otherwise DMV-like morphology present within a lysosomal compartment. **(H)** Tomogram slices at various z-heights showing a DMV with a microtubule trajectory nearby. **(I–J)** 3D model of the DMV and microtubule in H. **(K)** Box plot comparing number of DMVs per cytoplasmic area of the cell from a population of 50 cells for each group. Cells in the "12 hpi + CQ" group were treated with 100 μm chloroquine for the last 5 h of infection. Statistical significance was determined using the Wilcoxen rank sum test. **, $p \leq 0.01$. ***, $p \leq 0.001$.

protein localizes with the Golgi early in infection, and late in infection becomes distributed throughout the cell, including partial colocalization with the ER (Fig. 1B, Fig. S1). In the LVTs, four distinct membrane structures containing VPs were observed at both timepoints. Rough ER (Fig. 8A) and Golgi cisternae (Fig. 8B) were easily identifiable by morphology. VP were also found in the lumen of small smooth vesicles assumed to be ERGIC (Fig. 8C) (Tooze et al., 1984; Krijnse-Locker et al., 1994). Larger electron-lucent vesicles often containing many VP and other structures of varying morphology were also observed (Fig. 8D) (Ulasli et al., 2010). VP were mostly found fully enveloped in the lumen of organelles, while a proportion were in the process of assembly and/or budding (Fig. 6G and H). The organelle association of each VP in the two LVTs was tabulated. In the 7 hpi volume, a total of 391 VPs were identified (3.1 VP/μm^3). The majority of VP (70%) were located in small

vesicles (ERGIC), 15% in the Golgi, 12% in large vesicles, and 2% in the rough ER (Fig. 8E and G). In the 12 hpi LVT, 3202 virus particles were present (59.3 VP/μm^3), a 20-fold increase in density from the earlier timepoint. The majority of VP were in the lumen of the ER (89%), followed by the Golgi (5%), small vesicles (4.5%), and large vesicles (1%) (Fig. 8F and G). These numbers show that the period of MHV infection between 7 and 12 hpi involves a surge in VP assembly and envelopment, largely taking place on ER membranes. Overall, the Golgi and large vesicles are minor membrane sources for MHV envelopment throughout infection. The major budding compartment shifts from the ERGIC to the ER as infection progresses. This dynamic use of organelles for virus assembly occurs concurrently with the shift from formation of replication-associated DMVs to the degradation of the RVN.
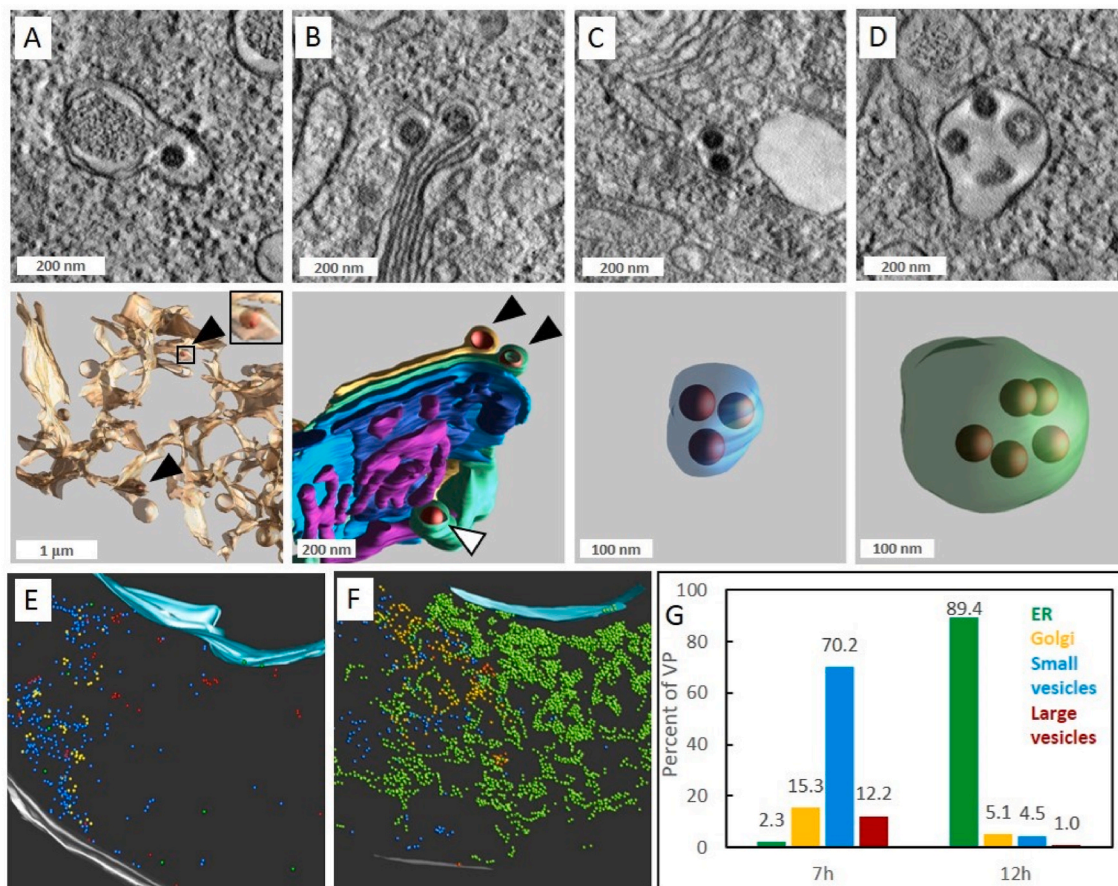
Fig. 8. Analysis of the virus budding compartment through the course of MHV infection. LVT from both 7 hpi and 12 hpi reveal enveloped VP within the interior of rough ER **(A)**, Golgi **(B)**, small vesicles **(C)** and larger electron lucent vacuoles **(D)**. The location of each VP within the 7 hpi volume **(E)** and the 12 hpi volume **(F)** is indicated, color-coded based on the compartment in which they are found: ER (green), Golgi (yellow), small vesicles (blue) and large vacuoles (red). **(G)** Comparison of the percentage of VP in each group at the two timepoints.

3. Discussion

In this work, we provide a comprehensive 3D ultrastructural analysis of the coronavirus RVN as well as new insights on its dynamic nature throughout infection. Utilizing large volume electron tomography, we first characterized the RVN as a vast network of DMVs, CMs, and ER which accumulates throughout infection and is broken down late in infection. We provide evidence that DMVs have a life-cycle consisting of budding from the ER and trafficking to lysosomes for degradation. Finally, we provide 3D quantitation showing that in addition to the changing nature of the RVN, virus assembly takes place preferentially in the ERGIC early in infection and the ER late in infection. Taken together, these analyses provide a broad view of the interaction of a coronavirus with its host cell organelles.

One long-standing question about CoV DMVs is the morphological mechanism of their formation. Two possible mechanisms have been proposed. The wrapping mechanism involves pairing of membranes followed by curving of the membranes into vesicular structures, followed by membrane fission events to separate the vesicle from the ER. The double budding mechanism involves invagination of the ER to form a vesicle inside the lumen, which subsequently buds out from the ER to acquire its second membrane. Several studies to date indicate that membrane pairing is most likely the first required step in CoV DMV biogenesis, mediated specifically by nsp3 and nsp4 (Angelini et al., 2013, 2014; Oudshoorn et al., 2017; van der Hoeven et al., 2016). From the cellular perspective, DMV formation is mediated by ERAD tuning, a budding process which can be observed in EM as exvaginations of the ER (Zuber et al., 2007). In this study we sought to maximize our chances of

observing formation intermediates which might indicate which of the two models or combination of them is most correct. We collected a volume with nearly 700 DMVs at a timepoint where the DMV formation rate is expected to be at its maximum (Ulasli et al., 2010). Although we observed large cisternal areas of paired ER, we found no evidence that paired regions wrap around to form DMVs, as in the biogenesis of autophagosomes or has been suggested for Arteriviruses (van der Hoeven et al., 2016; Hayashi-Nishino et al., 2010; Uemura et al., 2014). The morphologically earliest stage of DMV we observed were the "budding" DMVs, which were characterized by a fully formed inner vesicle, an outer membrane continuous with the ER, and extensive pairing of the inner and outer membrane aside from the connected region. Budding DMVs have similar structure to those observed in the distantly-related Arterivirus porcine reproductive and respiratory syndrome virus (Zhang et al., 2018). The formation mechanism for Arterivirus DMVs is still being explored, and tomographic evidence of potential intermediates exists for both the wrapping and double budding model (van der Hoeven et al., 2016). We found no morphological evidence of formation of the inner vesicle or accumulation of the inner density, indicating that the initial formation of DMVs is a rapid process. While our data cannot provide conclusive evidence for the earliest mechanism of DMV formation, it is clear that the final stage of formation is a budding event involving the pairing of the membranes in the neck-like connection the ER, which gives rise to the pinching DMV class. The final step involves fission of the membranes to separate from the ER/RVN.

While our work is in agreement with previous studies that show that DMVs are largely connected within the RVN (Knoops et al., 2008; Wolff

et al., 2020), we show that 19% of MHV DMVs are bona-fide vesicles which are separate from the RVN, and that DMVs are trafficked to lysosomes for degradation. DMVs thus appear to follow the ERAD tuning pathway in its entirety. While the connection of the formation of DMVs to the ERAD tuning pathway has been established (Reggiori et al., 2010), it has been assumed that the increase in DMV numbers over time as well as the decreased turnover of EDEM1 indicate that the virus stalls or stops the ERAD tuning pathway (Ulasli et al., 2010; Reggiori et al., 2010). Our work challenges that notion by looking at later timepoints in infection. By 12 hpi, the decrease in the number of DMVs is noticeable. By 16 hpi, it is difficult to find a single DMV, let alone a cluster of DMVs, suggesting that this degradative process continues through infection. Our observations are in agreement with findings from another Nidovirus, EAV, in which the amount of dsRNA decreases during the last two-thirds of the observed infection (Monastyrska et al., 2013). EAV DMVs also form from the ERAD tuning pathway (Monastyrska et al., 2013), so it is tempting to speculate that they have a similar degradative fate as those of MHV. It is possible that this degradation of replication proteins and RNA may be a theme in other viruses as well, as the role of ERAD proteins has also been established for a flavivirus (Sharma et al., 2014) and a coxsackievirus (Alirezaei et al., 2015).

The trafficking of individual DMVs is consistent with live cell imaging indicating that MHV nsp2-labeled structures are present in two distinct populations, one of which was of smaller size and mobile, and the other which were larger in size and immobile (Hagemeijer et al., 2010). Similar dynamics of ER-derived replication complexes in hepatitis C virus (HCV) have been observed by live cell imaging (Wolk et al., 2008). While the ultrastructure corresponding with the two populations were not visualized, it was assumed that the small structures were individual DMVs traveling toward the perinuclear DMV/CM clusters where they become immobilized. While this directionality is possible, our data indicates that at least a portion of DMVs are trafficking away from the RVN toward lysosomes. Interestingly, a study published during the revision of this manuscript found that lysosomes are involved in CoV egress through a lysosomal exocytosis pathway (Ghosh et al., 2020). Virus-laden lysosomes were shown to fuse with the plasma membrane and release their contents. Since our data indicates that DMVs are also present in lysosomes, it is possible that DMV numbers decrease due to expulsion from the cell rather than lysosomal degradation.

In addition to role of the ER in the formation of the RVN, the ER plays a role in MHV envelopment. Because both replication and assembly involve membrane proteins that must be processed through the ER, the processes occur somewhat simultaneously, but involve different morphologies and proteins. Virally-encoded nonstructural proteins together form DMVs (Angelini et al., 2013; Oudshoorn et al., 2017), which are produced by budding out from the ER. In contrast, envelopment of new virus particles produces negative curvature of the ER into its lumen, mediated by the structural proteins M, E, and S (de Haan and Rottier, 2005). We have demonstrated that these two processes in the ER are largely separated in time, with DMV formation being the dominant process in the ER up to around 10 hpi. By 12 hpi, the ER is extensively involved in the assembly process, and DMV formation has slowed or stopped altogether. These observations raise questions as to what governs the rapid switchover in the role of the ER. Is it primarily controlled by the cell or by the virus? Does the slowing of replication late in infection allow the ER to be used for assembly? Or does the translation of vast quantities of structural proteins in effect edge out the nonstructural proteins, causing DMV production to slow? Or do the structural proteins and thus the assembly process "back up" into the ER due to the virus particles budding downstream in the secretory pathway? Additionally, the large capacity of the ER compared with the ERGIC and Golgi raises questions about the logistics of processing such large numbers of viruses through the remainder of the secretory pathway. Perhaps many of the ER-budded VP are not released from the cell or perhaps CoV utilize a non-conventional pathway from the ER out of the cell.

Overall, this work provides morphological definition to the dynamic

rearrangements of the ER by a coronavirus. We show that the DMV lifecycle includes budding from the ER, association with the RVN, separating from the RVN and trafficking to the lysosome for degradation (Fig. 9). The formation and degradation rates are such that through the infection, the number of DMVs increases early in infection, followed by a dramatic decrease between 10 and 12 hpi. Concurrent with the RVN breakdown, virus assembly on the ER is increasing rapidly, necessitating major structural changes to the organelle. While our work here is based on ultrastructural imaging, it opens up a multitude of questions that can be addressed by other techniques. Future understanding of what controls the DMV degradation rate, or what causes the ER to suddenly begin assembling thousands of new virions could provide the basis for new strategies to combat coronavirus infection.

4. Materials and methods

4.1. Virus and cells

Murine 17Cl-1 fibroblasts (Sturman and Takemoto, 1972) were cultured in Dulbecco's modified Eagle's medium (DMEM) supplemented with 5% fetal bovine serum (FBS), 10% Tryptose phosphate broth, and Pen/Strep at 37 °C in a 5% CO_2 atmosphere. Cells were infected with mouse hepatitis virus strain A59 (Robb and Bond, 1979) (MHV-A59) at multiplicities of infection (m.o.i.) between 0.1 and 10 as indicated. MHV-A59 expressing green fluorescent protein as a fusion with the replicase protein nsp3 (MHV-Δ2-GFP3 (Freeman et al., 2014)) was used for fluorescence imaging. For the viral growth curve, 17Cl-1 cells were infected with MHV-A59 at an m.o.i. of 10. At the indicated timepoints post infection, the media was collected and virus titers were determined by plaque assay. Triplicate wells were prepared for each timepoint: 4, 7, 10, 12, and 16 hpi.

4.2. Immunofluorescence microscopy

17Cl-1 cells were grown on glass coverslips and infected with MVH-A59 or MHV-Δ2-GFP3 at an m.o.i. of 0.1. At various times post infection between 4 and 16 h, cell monolayers were washed in phosphate buffered saline (PBS), fixed with 100% methanol for 15 min at −20 °C, washed in PBS, and blocked overnight at 4 °C in 0.2% cold water fish skin gelatin in PBS. Cells were incubated with primary antibodies for 2 h at room temperature, followed by washing, incubation in secondary antibodies for 1 h, and final washes. Coverslips were mounted on glass slides using FluorSave reagent (Calbiochem) prior to imaging. Primary antibodies used were mouse monoclonal *anti*-M J1.3 (Fleming et al., 1989), rabbit polyclonal *anti*-calreticulin and rabbit monoclonal *anti*-Golgin-97 (Cell Signaling Technology). Goat anti-mouse FITC and goat anti-rabbit Texas Red (Invitrogen) were used as secondary antibodies. Confocal imaging was performed on a Nikon A1RMP laser scanning confocal microscope equipped with 488 nm and 561 nm lasers, using a 60× oil immersion objective with numerical aperture 1.4. Multi-channel imaging was performed sequentially for each laser, with line averaging of 2, utilizing the full 4k x 4k pixel CCD. NIS Elements software (Nikon) was used for data collection, and Fiji ImageJ was used for image cropping, channel overlay, and line intensities (Abràmoff et al., 2004; Schindelin et al., 2012).

4.3. Preparation of cells for electron microscopy and tomography

At the timepoints indicated in the text, MHV-A59-infected 17Cl-1 cells were washed with PBS, then incubated for 5 min with 0.25% Trypsin-EDTA (Corning). Cells were pelleted at 500×g, resuspended in a cryoprotectant of 20% bovine serum albumin in DMEM, and pelleted again. A small volume (2–3 μl) of the resulting cell pellet was loaded into the well of a 1.5 mm × 0.1 mm membrane carrier (Mager Scientific) and cryo-fixed using the EM PACT2 high pressure freezer (Leica). Cryo-fixed cells were processed by freeze substitution (FS) using an AFS2 automated freeze substitution unit (Leica). Briefly, frozen cell samples were
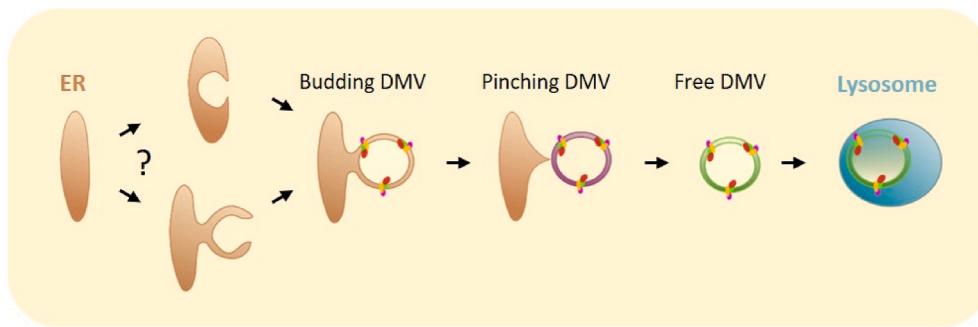
Fig. 9. Morphological model of a DMV life-cycle. Our model proposes that first, the inner DMV vesicle is formed within the ER by one of several possible topologically-equivalent processes, followed by budding out of the ER to obtain a second membrane. DMVs may remain connected to the ER and the RVN via pinching connections for some time before separating to become free DMVs. Free DMVs are trafficked through the cytoplasm on MTs and merge with the lysosome for degradation. Together these steps describe a morphological birth, lifetime, and death of a DMV.

incubated at −90 °C in a solution of tannic acid in acetone, followed by slowly warming to room temperature in a solution of uranyl acetate and osmium tetroxide in acetone (chemicals from Electron Microscopy Sciences). Over 30 cell preparation conditions were tested before choosing a cell line, FS chemical mix, and FS warming protocol which gave optimal preservation of virus-derived membrane rearrangements and membrane staining suitable for electron tomography. After FS, samples were infiltrated with Durcupan ACM resin (Sigma-Aldrich), and blocks were polymerized at 60 °C. Ultrimicrotomy was performed using an UC7 ultramicrotome (Leica).

For CQ treatment, cells were infected as described above with MHV-A59 at m.o.i. 10. At 7 hpi, 5 μl of cell media was removed and replaced by a 20 mM solution of chloroquine diphosphate (Sigma-Aldrich) in DI water. The total CQ concentration was 100 μM. After 5 h of CQ treatment (12 hpi), cells were cryofixed and processed for EM.

4.4. Electron microscopy of thin sections

Thin sections (90 nm) were used for screening and quantitative analysis of cell cross sections in 2D. Sections were collected on formvar-coated copper slot grids and contrasted with 2% aqueous uranyl acetate and Sato's lead. Imaging was performed on a Philips CM-100 microscope operating at 100 kV or a Tecnai T12 microscope operating at 80 kV, both equipped with a Gatan Orius CCD camera. For quantitative analysis, 25 cross sections of infected cells were imaged. For each infected cell, a series of overlapping images were collected covering the entire cell cross section at a magnification high enough to identify DMVs and virus particles. Images were montaged together using the MosiacJ plugin of ImageJ (Thévenaz and Unser, 2007), and the montage of each cell was imported into IMOD (Kremer et al., 1996). The plasma membrane and nucleus were hand traced as single contours, and the locations of DMVs and virus particles were marked using point objects. Cytoplasmic area was determined by subtracting the area inside the nuclear trace from the area inside the plasma membrane trace. DMV density was determined as the number of DMVs counted per μm^2 of cytoplasmic area. Statistical significance between groups was determined using the Wilcoxen rank sum test.

4.5. Large volume electron tomography

Serial sections of 250 nm thickness were collected on LUXFilm coated 2 × 1 mm copper slot grids (Luxel). Sections were contrasted with 2% aqueous uranyl acetate and Sato's lead before carbon coating and overlaying with 10-nm colloidal gold particles (Sigma) for use as fiducial markers. Grids were screened on the Philips CM100 or Tecnai T12 microscope for representative cells. LVT were collected using a Titan Krios TEM (FEI) operating at 300 kV at room temperature. Tilt series were collected with automation using SerialEM (Mastronarde, 2003). First, a low magnification image montage of the entire grid was created to use as a map for marking regions of interest. The area of interest in a cell was visualized and marked on consecutive serial sections. At each section, a tilt series was collected. For each tilt series, images were collected at tilts

from +60 to - 60° in 2° increments. To increase the area imaged, a 2 × 2 image montage was collected at each tilt. The datasets for the 7 hpi and 12 hpi timepoints were collected on different cameras due to the replacement of the CCD camera with a direct electron detector by the Purdue Cryo-EM facility between the collections of the two datasets. Every effort was made to collect as similar datasets as possible; however, differences in image size and collection parameters, as well as reconstruction, were unavoidable, and are described below.

The 7 hpi dataset was collected using a 4k x 4k pixel UltraScan 4000 CCD camera (Gatan). Montage images were collected at a magnification corresponding to 1 nm/pixel at the specimen level. Final image dimensions were 7800 × 7800 pixels due to the 200 pixel overlap of the montage. Eight serial sections of a region of a cell were imaged. Images were aligned using cubic interpolation and tomograms reconstructed by weighted back projection using IMOD.

The 12 hpi dataset was collected on the K2 direct electron detector (Gatan) operating in linear mode at 95% of the maximum dose rate. Montage images were collected at a magnification corresponding to 0.8 nm/pixel at the specimen level. Final image dimensions were 7296 × 7040 pixels. Five serial sections of a region of a cell were imaged. Images were binned by 2 and aligned using linear interpolation. Reconstruction of tomograms was done in IMOD using 30 iterations of SIRT.

For each dataset, serial tomograms were aligned and joined in z to produce reconstructed volumes with dimensions 7.8 × 7.8 × 2 μm (7 hpi) and 5.8 × 5.6 × 1.25 μm (12 hpi). DMVs were segmented by hand tracing using IMOD's Drawing Tools and Interpolator, and 3D surface models were generated by meshing. Virus particles and budding virus were approximated by placing a sphere with a radius corresponding to a diameter of 90 nm at the center of each virus particle density. The ER and Golgi were segmented via semi-automated methods using Microscopy Image Browser (Belevich et al., 2016). A combination of watershed segmentation using superpixels and the "Membrane Clicker" tool were used to delineate membranes of interest. Model data was transferred into IMOD, smoothed and meshed to produce 3D models.

Appendix A. Supplementary data

Supplementary data related to this article can be found at https://doi.org/10.1016/j.virol.2020.12.007.

References

Abràmoff, M.D., Magalhães, P.J., Ram, S.J., 2004. Image processing with ImageJ. Biophot. Int. 11, 36–41.

Alirezaei, M., Flynn, C.T., Wood, M.R., Harkins, S., Whitton, J.L., 2015. Coxsackievirus can exploit LC3 in both autophagy-dependent and -independent manners in vivo. Autophagy 11, 1389–1407.

Angelini, M.M., Akhlaghpour, M., Neuman, B.W., 2013. Severe acute respiratory syndrome coronavirus nonstructural proteins 3, 4, and 6 induce double-membrane vesicles. mBio 4 e00524-13.

Angelini, M.M., Neuman, B.W., Buchmeier, M.J., 2014. Untangling membrane rearrangement in the nidovirales. DNA Cell Biol. 33, 122–127.

Belevich, I., Joensuu, M., Kumar, D., Vihinen, H., Jokitalo, E., 2016. Microscopy image browser: a platform for segmentation and analysis of multidimensional datasets. PLoS Biol. 14, 1–13.

Bernasconi, R., Pertel, T., Luban, J., Molinari, M., 2008. A dual task for the Xbp1-responsive OS-9 variants in the mammalian endoplasmic reticulum: inhibiting secretion of misfolded protein conformers and enhancing their disposal. J. Biol. Chem. 283, 16446–16454.

Calì, T., Galli, C., Olivari, S., Molinari, M., 2008. Segregation and rapid turnover of EDEM1 by an autophagy-like mechanism modulates standard ERAD and folding activities. Biochem. Biophys. Res. Commun. 371, 405–410.

Christianson, J.C., Shaler, T.A., Tyler, R.E., Kopito, R.R., 2008. OS-9 and GRP94 deliver mutant α1-antitrypsin to the Hrd1-SEL1L ubiquitin ligase complex for ERAD. Nat. Cell Biol. 10, 272–282.

Doyle, N., Hawes, P.C., Simpson, J., Adams, L.H., Maier, H.J., 2019. The porcine deltacoronavirus replication organelle comprises double-membrane vesicles and zippered endoplasmic reticulum with double-membrane spherules. Viruses 11 11 (11), 1030–1045.

Fleming, J.O., Shubin, R.A., Sussman, M.A., Casteel, N., Stohlman, S.A., 1989. Monoclonal antibodies to the matrix (E1) glycoprotein of mouse hepatitis virus protect mice from encephalitis. Virology 168, 162–167.

Fourn, V Le, Guhl, B., Santimaria, R., Zuber, C., Roth, J., 2009. Basal autophagy is involved in the degradation of the ERAD component EDEM1. Cell. Mol. Life Sci. 66, 1434–1445.

Freeman, M.C., Graham, R.L., Lu, X., Peek, C.T., Denison, M.R., 2014. Coronavirus replicase-reporter fusions provide quantitative analysis of replication and replication complex formation. J. Virol. 88, 5319–5327.

Ghosh, S., Dellibovi-Ragheb, T.A., Kerviel, A., Pak, E., Qiu, Q., Fisher, M., Takvorian, P. M., Bleck, C., Hsu, V.W., Fehr, A.R., Perlman, S., Achar, S.R., Straus, M.R., Whittaker, G.R., de Haan, C.A.M., Kehrl, J., Altan-Bonnet, G., Altan-Bonnet, N., 2020. β-Coronaviruses use lysosomes for egress instead of the biosynthetic secretory pathway. Cell 1–16.

Goldsmith, C.S., Tatti, K.M., Ksiazek, T.G., Rollin, P.E., Comer, J.A., Lee, W.W., Rota, P. A., Bankamp, B., Bellini, W.J., Zaki, S.R., 2004. Ultrastructural characterization of SARS coronavirus. Emerg. Infect. Dis. 10, 320–326.

Gosert, R., Kanjanahaluethai, A., Egger, D., Bienz, K., Baker, S.C., 2002. RNA replication of mouse hepatitis virus takes place at double-membrane vesicles. J. Virol. 76, 3697–3708.

De Groot, R.J., Van Leen, R.W., Dalderup, M.J., Vennema, H., Horzinek, M.C., Spaan, W. J., 1989. Stably expressed FIPV peplomer protein induces cell fusion and elicits neutralizing antibodies in mice. Virology 171, 493–502.

de Haan, C.A.M., Rottier, P.J.M., 2005. Molecular interactions in the assembly of coronaviruses. Adv. Virus Res. 64, 165–230.

Hagemeijer, M.C., Verheije, M.H., Ulasli, M., Shaltiël, I.A., Vries, LA De, Reggiori, F., Rottier, P.J.M., de Haan, C.A.M., 2010. Dynamics of coronavirus replication-transcription complexes. J. Virol. 84, 2134–2149.

Harcourt, B.H., Jukneliene, D., Kanjanahaluethai, A., Bechill, J., Severson, K.M., Smith, C.M., Rota, P.A., Baker, S.C., 2004. Identification of severe acute respiratory syndrome coronavirus replicase products and characterization of papain-like protease activity. J. Virol. 78, 13600–13612.

Hayashi-Nishino, M., Fujita, N., Noda, T., Yamaguchi, A., Yoshimori, T., Yamamoto, A., 2010. Electron tomography reveals the endoplasmic reticulum as a membrane source for autophagosome formation. Autophagy 6, 301–303.

van der Hoeven, B., Oudshoorn, D., Koster, A.J., Snijder, E.J., Kikkert, M., Bárcena, M., 2016. Biogenesis and architecture of arterivirus replication organelles. Virus Res. 220, 70–90.

Kanjanahaluethai, A., Chen, Z., Jukneliene, D., Baker, S.C., 2007. Membrane topology of murine coronavirus replicase nonstructural protein 3. Virology 361, 391–401.

Klein, S., Cortese, M., Winter, S., Wachsmuth-Melm, M., Neufeldt, C., Cerikan, B., Stanifer, M., Boulant, S., Bartenschlager, R., Chlanda, P., 2020. SARS-CoV-2 structure and replication characterized by in situ cryo-electron tomography. Nat. Commun. 1–10.

Knoops, K., Kikkert, M., van den Worm, S.H.E., Zevenhoven-Dobbe, J.C., van der Meer, Y., Koster, A.J., Mommaas, A.M., Snijder, E.J., 2008. SARS-coronavirus replication is supported by a reticulovesicular network of modified endoplasmic reticulum. PLoS Biol. 6, e226.

Kremer, J.R., Mastronarde, D.N., McIntosh, J.R., 1996. Computer visualization of three-dimensional image data using IMOD. J. Struct. Biol. 116, 71–76.

Krijnse-Locker, J., Ericsson, M., Rottier, P.J.M., Griffiths, G., 1994. Characterization of the budding compartment of mouse hepatitis virus: evidence that transport from the RER to the Golgi complex requires only one vesicular transport step. J. Cell Biol. 124, 55–70.

Maier, H.J., Hawes, P.C., Cottam, E.M., Mantell, J., Verkade, P., Monaghan, P., Wileman, T., Britton, P., 2013. Infectious bronchitis virus generates spherules from zippered endoplasmic reticulum membranes. mBio 4.

Mastronarde, D., 2003. SerialEM: a program for automated tilt series acquisition on Tecnai microscopes using prediction of specimen position. Microsc. Microanal. 9, 1182–1183.

Molinari, M., Calanca, V., Galli, C., Lucca, P., Paganetti, P., 2003. Role of EDEM in the release of misfolded glycoproteins from the calnexin cycle. Science 299 (80), 1397–1400.

Monastyrska, I., Ulasli, M., Rottier, P.J.M., Guan, J.L., Reggiori, F., De Haan, C.A.M., 2013. An autophagy-independent role for LC3 in equine arteritis virus replication. Autophagy 9, 164–174.

Nixon-Abell, J., Obara, C.J., Weigel, A.V., Li, D., Legant, W.R., Xu, C.S., Pasolli, H.A., Harvey, K., Hess, H.F., Betzig, E., Blackstone, C., Lippincott-Schwartz, J., 2016. Increased spatiotemporal resolution reveals highly dynamic dense tubular matrices in the peripheral ER. Science 80, 354.

Noske, A.B., Costin, A.J., Morgan, G.P., Marsh, B.J., 2008. Expedited approaches to whole cell electron tomography and organelle mark-up in situ in high-pressure frozen pancreatic islets. J. Struct. Biol. 161, 298–313.

Oda, Y., Hosokawa, N., Wada, I., Nagata, K., 2003. EDEM as an acceptor of terminally misfolded glycoproteins released from calnexin. Science 299 (80), 1394–1397.

Oostra, M., te Lintelo, E.G., Deijs, M., Verheije, M.H., Rottier, P.J.M., de Haan, C.A.M., 2007. Localization and membrane topology of coronavirus nonstructural protein 4: involvement of the early secretory pathway in replication. J. Virol. 81, 12323–12336.

Oostra, M., Hagemeijer, M.C., van Gent, M., Bekker, C.P.J., te Lintelo, E.G., Rottier, P.J. M., de Haan, C. a M., 2008. Topology and membrane anchoring of the coronavirus replication complex: not all hydrophobic domains of nsp3 and nsp6 are membrane spanning. J. Virol. 82, 12392–12405.

Oudshoorn, D., Rijs, K., Limpens, R.W.A.L., Groen, K., Koster, A.J., Snijder, E.J., Kikkert, M., Bárcena, M., 2017. Expression and cleavage of middle east respiratory syndrome nsp3-4 polyprotein induce the formation of double-membrane vesicles that mimic those associated with coronaviral RNA replication. mBio 8, 1–17.

Puhka, M., Vihinen, H., Joensuu, M., Jokitalo, E., 2007. Endoplasmic reticulum remains continuous and undergoes sheet-to-tubule transformation during cell division in mammalian cells. J. Cell Biol. 179, 895–909.

Puhka, M., Joensuu, M., Vihinen, H., Belevich, I., Jokitalo, E., 2012. Progressive sheet-to-tubule transformation is a general mechanism for endoplasmic reticulum partitioning in dividing mammalian cells. Mol. Biol. Cell 23, 2424–2432.

Reggiori, F., Monastyrska, I., Verheije, M.H., Calì, T., Ulasli, M., Bianchi, S., Bernasconi, R., de Haan, C.A.M.M., Molinari, M., 2010. Coronaviruses hijack the LC3-I-positive EDEMosomes, ER-derived vesicles exporting short-lived ERAD regulators, for replication. Cell Host Microbe 7, 500–508.

Robb, J.A., Bond, C.W., 1979. Pathogenic murine coronaviruses I. Characterization of biological behavior in vitro and virus-specific intracellular RNA of strongly neurotropic JHMV and weakly neurotropic A59V viruses. Virology 94, 352–370.

Romero-Brey, I., Bartenschlager, R., 2014. Membranous replication factories induced by plus-strand RNA viruses. Viruses 6, 2826–2857.

Schindelin, J., Arganda-Carreras, I., Frise, E., Kaynig, V., Longair, M., Pietzsch, T., Preibisch, S., Rueden, C., Saalfeld, S., Schmid, B., Tinevez, J.Y., White, D.J., Hartenstein, V., Eliceiri, K., Tomancak, P., Cardona, A., 2012. Fiji: an open-source platform for biological-image analysis. Nat. Methods 9, 676–682.

Sharma, M., Bhattacharyya, S., Nain, M., Kaur, M., Sood, V., Gupta, V., Khasa, R., Abdin, M.Z., Vrati, S., Kalia, M., 2014. Japanese encephalitis virus replication is negatively regulated by autophagy and occurs on LC3-I- and EDEM1-containing membranes. Autophagy 10, 1637–1651.

Snijder, E.J., van der Meer, Y., Zevenhoven-Dobbe, J., Onderwater, J.J.M., van der Meulen, J., Koerten, H.K., Mommaas, a M., 2006. Ultrastructure and origin of membrane vesicles associated with the severe acute respiratory syndrome coronavirus replication complex. J. Virol. 80, 5927–5940.

Snijder, E.J., Limpens, R.W.A.L., de Wilde, A.H., de Jong, A.W.M., Zevenhoven-Dobbe, J. C., Maier, H.J., Faas, F.G.A., Koster, A.J., Bárcena, M., 2020. A unifying structural and functional model of the coronavirus replication organelle: tracking down RNA synthesis. PLoS Biol. 18, e3000715.

Sturman, L.S., Takemoto, K.K., 1972. Enhanced growth of a murine coronavirus in transformed mouse cells. Infect. Immun. 6, 501–507.

Sturman, L.S., Holmes, K.V., Behnke, J., 1980. Isolation of coronavirus envelope glycoproteins and interaction with the viral nucleocapsid. J. Virol. 33, 449–462.

Thévenaz, P., Unser, M., 2007. User-friendly semiautomated assembly of accurate image mosaics in microscopy. Microsc. Res. Tech. 70, 135–146.

Tooze, J., Tooze, S., Warren, G., 1984. Replication of coronavirus MHV-A59 in sac- cells: determination fo the first site of budding of progeny virions. Eur. J. Cell Biol. 33, 281–293.

Uemura, T., Yamamoto, M., Kametaka, A., Sou, Y., Yabashi, A., Yamada, A., Annoh, H., 2014. A cluster of thin tubular structures mediates transformation of the endoplasmic reticulum to autophagic isolation membrane. Mol. Cell Biol. 34, 1695–1706.

Ulasli, M., Verheije, M.H., de Haan, C.A.M., Reggiori, F., 2010. Qualitative and quantitative ultrastructural analysis of the membrane rearrangements induced by coronavirus. Cell Microbiol. 12, 844–861.

Verheije, M.H., Raaben, M., Mari, M., Te Lintelo, E.G., Reggiori, F., Van Kuppeveld, F.J. M., Rottier, P.J.M., De Haan, C. a M., 2008. Mouse hepatitis coronavirus RNA replication depends on GBF1-mediated ARF1 activation. PLoS Pathog. 4, e1000088.

West, M., Zurek, N., Hoenger, A., Voeltz, G.K., 2011. A 3D analysis of yeast ER structure reveals how ER domains are organized by membrane curvature. J. Cell Biol. 193, 333–346.

de Wilde, A.H., Raj, V.S., Oudshoorn, D., Bestebroer, T.M., van Nieuwkoop, S., Limpens, R.W.A.L., Posthuma, C.C., van der Meer, Y., Bárcena, M., Haagmans, B.L., Snijder, E.J., van den Hoogen, B.G., 2013. MERS-coronavirus replication induces severe in vitro cytopathology and is strongly inhibited by cyclosporin A or interferon-α treatment. J. Gen. Virol. 94, 1749–1760.

Wolff, G., Limpens, R.W.A.L., Zevenhoven-Dobbe, J.C., Laugks, U., Zheng, S., de Jong, A. W.M., Koning, R.I., Agard, D.A., Grünewald, K., Koster, A.J., Snijder, E.J., Bárcena, M., 2020. A molecular pore spans the double membrane of the coronavirus replication organelle. Science 369 (80), 1395–1398.

Wolk, B., Buchele, B., Moradpour, D., Rice, C.M., 2008. A dynamic view of hepatitis C virus replication complexes. J. Virol. 82, 10519–10531.

van den Worm, S.H.E., Knoops, K., Zevenhoven-Dobbe, J.C., Beugeling, C., van der Meer, Y., Mommaas, a M., Snijder, E.J., 2011. Development and RNA-synthesizing activity of coronavirus replication structures in the absence of protein synthesis. J. Virol. 85, 5669–5673.

Zhang, W., Chen, K., Zhang, X., Guo, C., Chen, Y., Liu, X., 2018. An integrated analysis of membrane remodeling during porcine reproductive and respiratory syndrome virus replication and assembly. PloS One 13, 1–18.

Zuber, C., Cormier, J.H., Guhl, B., Santimaria, R., Hebert, D.N., Roth, J., 2007. EDEM1 reveals a quality control vesicular transport pathway out of the endoplasmic reticulum not involving the COPII exit sites. Proc. Natl. Acad. Sci. U. S. A. 104, 4407–4412.